JGR Atmospheres

RESEARCH ARTICLE
10.1029/2024JD040978

Seasonal and Local Time Variation in the Observed Peak of the Meteor Altitude Distributions by Meteor Radars

E. C. M. Dawkins[1,2], D. Janches[1], G. Stober[3], J. D. Carrillo-Sánchez[1,2], R. S. Lieberman[1], C. Jacobi[4], T. Moffat-Griffin[5], N. J. Mitchell[5,6], N. Cobbett[5], P. P. Batista[7], V. F. Andrioli[7,8], R. A. Buriti[9], D. J. Murphy[10], J. Kero[11], N. Gulbrandsen[12], M. Tsutsumi[13,14], A. Kozlovsky[15], M. Lester[16], J.-H. Kim[17], C. Lee[17], A. Liu[18], B. Fuller[19], D. O'Connor[19], S. E. Palo[20], M. J. Taylor[21], J. Marino[22], and N. Rainville[20]

[1]ITM Physics Laboratory, NASA Goddard Space Flight Center, Greenbelt, MD, USA, [2]Department of Physics, Catholic University of America, Washington, DC, USA, [3]University Bern, Institute of Applied Physics, Bern, Switzerland, [4]Institute for Meteorology, Leipzig University, Leipzig, Germany, [5]British Antarctic Survey, Cambridge, UK, [6]University of Bath, Bath, UK, [7]National Institute for Space Research (INPE), São José dos Campos, Brazil, [8]China-Brazil Joint Laboratory for Space Weather, NSSC/INPE, São José dos Campos, Brazil, [9]Department of Physics, Federal University of Campina Grande, Campina Grande, Brazil, [10]Australian Antarctic Division, Kingston, TAS, Australia, [11]Swedish Institute of Space Physics (IRF), Kiruna, Sweden, [12]Tromsø Geophysical Observatory, UiT - The Arctic University of Norway, Tromsø, Norway, [13]National Institute of Polar Research, Tachikawa, Japan, [14]The Graduate University for Advanced Studies (SOKENDAI), Tokyo, Japan, [15]Sodankylä Geophysical Observatory, University of Oulu, Oulu, Finland, [16]Department of Physics and Astronomy, University of Leicester, Leicester, UK, [17]Division of Atmospheric Sciences, Korea Polar Research Institute, Incheon, South Korea, [18]Center for Space and Atmospheric Research and Department of Physical Sciences, Embry-Riddle Aeronautical University, Daytona Beach, FL, USA, [19]Genesis Software, Pty Ltd., Adelaide, SA, Australia, [20]Colorado Center for Astrodynamics Research (CCAR), Ann and H.J. Smead Aerospace Engineering Sciences, College of Engineering and Applied Sciences, University of Colorado Boulder, Boulder, CO, USA, [21]Department of Physics, Utah State University, Logan, UT, USA, [22]University of Colorado at Boulder, Boulder, CO, USA

Abstract Meteoroids of sub-milligram sizes burn up high in the Earth's atmosphere and cause streaks of plasma trails detectable by meteor radars. The altitude at which these trails, or meteors, form depends on a number of factors including atmospheric density and the astronomical source populations from which these meteoroids originate. A previous study has shown that the altitude of these meteors is affected by long-term linear trends and the 11-year solar cycle related to changes in our atmosphere. In this work, we examine how shorter diurnal and seasonal variations in the altitude distribution of meteors are dependent on the geographical location at which the measurements are performed. We use meteoroid altitude data from 18 independent meteor radar stations at a broad range of latitudes and investigate whether there are local time (LT) and seasonal variations in the altitude of the peak meteor height, defined as the majority detection altitude of all meteors within a certain period, which differ from those expected purely from the variation in the visibility of their astronomical source. We find a consistent LT and seasonal response for the Northern Hemisphere locations regardless of latitude. However, the Southern Hemisphere locations exhibit much greater LT and seasonal variation. In particular, we find a complex response in the four stations located within the Southern Andes region, which indicates that the strong dynamical atmospheric activity, such as the gravity waves prevalent here, disrupts, and masks the seasonality and dependence on the astronomical sources.

Plain Language Summary Small meteoroids burn up high in the Earth's atmosphere producing trails of plasma detectable by ground-based meteor radar instruments. The altitude at which these trails occur depends on a number of factors including atmospheric density and the astronomical source populations from which these meteoroids originate. Previous work demonstrated that the altitude at which the majority of these meteoroids burn up (termed "peak meteor altitude") is affected by long-term atmospheric changes, such as those related to greenhouse gas emissions and the 11-year solar cycle. Here, we focus on shorter timescales and analyze meteoroid altitude data from 18 geographically diverse meteor radars to examine the local time (LT) and seasonal variation in the peak meteor altitudes on a latitude basis. We find a consistent LT and seasonal response among the six Northern Hemisphere meteor radar station locations irrespective of latitude. However, we find a more complex response among the 12 Southern Hemisphere stations with much greater LT and seasonal variation. In particular, we found a complex response in the four stations located within the Southern Andes region, a

Key Points:

- Local time (LT) and seasonal variations in the peak meteor height exist, which differ from those expected from astronomical variation alone
- There is a consistent LT and seasonal response in the Northern Hemisphere locations regardless of latitude
- A complex response in the Andes region where a strong gravity wave component acts to mask seasonality and dependence on astronomical sources

Correspondence to:
E. C. M. Dawkins,
erin.dawkins@nasa.gov

Citation:
Dawkins, E. C. M., Janches, D., Stober, G., Carrillo-Sánchez, J. D., Lieberman, R. S., Jacobi, C., et al. (2024). Seasonal and local time variation in the observed peak of the meteor altitude distributions by meteor radars. *Journal of Geophysical Research: Atmospheres*, *129*, e2024JD040978. https://doi.org/10.1029/2024JD040978

Received 13 FEB 2024
Accepted 12 OCT 2024

Author Contributions:
Conceptualization: E. C. M. Dawkins, D. Janches, G. Stober
Data curation: E. C. M. Dawkins, D. Janches, G. Stober, R. S. Lieberman, C. Jacobi, T. Moffat-Griffin, N. J. Mitchell, N. Cobbett, P. P. Batista, V. F. Andrioli, R. A. Buriti, D. J. Murphy, J. Kero, N. Gulbrandsen, M. Tsutsumi, A. Kozlovsky, M. Lester, J.-H. Kim, C. Lee, A. Liu, B. Fuller, D. O'Connor, S. E. Palo, M. J. Taylor, J. Marino, N. Rainville
Formal analysis: E. C. M. Dawkins, D. Janches, G. Stober, J. D. Carrillo-Sánchez
Funding acquisition: D. Janches, G. Stober
Investigation: E. C. M. Dawkins, D. Janches, G. Stober, J. D. Carrillo-Sánchez

Methodology: E. C. M. Dawkins, D. Janches, G. Stober
Resources: E. C. M. Dawkins, D. Janches, G. Stober, R. S. Lieberman, C. Jacobi, T. Moffat-Griffin, N. J. Mitchell, N. Cobbett, P. P. Batista, V. F. Andrioli, R. A. Buriti, D. J. Murphy, J. Kero, N. Gulbrandsen, M. Tsutsumi, A. Kozlovsky, M. Lester, J.-H. Kim, C. Lee, A. Liu, B. Fuller, D. O'Connor, S. E. Palo, M. J. Taylor, J. Marino, N. Rainville
Software: E. C. M. Dawkins, D. Janches, G. Stober
Validation: E. C. M. Dawkins, D. Janches, G. Stober, J. D. Carrillo-Sánchez
Visualization: E. C. M. Dawkins, D. Janches, G. Stober
Writing – original draft: E. C. M. Dawkins, D. Janches, G. Stober, J. D. Carrillo-Sánchez, R. S. Lieberman, C. Jacobi, T. Moffat-Griffin, N. J. Mitchell, N. Cobbett, P. P. Batista, V. F. Andrioli, R. A. Buriti, D. J. Murphy, J. Kero, N. Gulbrandsen, M. Tsutsumi, A. Kozlovsky, M. Lester, J.-H. Kim, C. Lee, A. Liu, B. Fuller, D. O'Connor, S. E. Palo, M. J. Taylor, J. Marino, N. Rainville
Writing – review & editing: E. C. M. Dawkins, D. Janches, G. Stober, J. D. Carrillo-Sánchez, R. S. Lieberman, C. Jacobi, T. Moffat-Griffin, N. J. Mitchell, N. Cobbett, P. P. Batista, V. F. Andrioli, R. A. Buriti, D. J. Murphy, J. Kero, N. Gulbrandsen, M. Tsutsumi, A. Kozlovsky, M. Lester, J.-H. Kim, C. Lee, A. Liu, B. Fuller, D. O'Connor, S. E. Palo, M. J. Taylor, J. Marino, N. Rainville

geographic region known for intense atmospheric gravity wave activity, which acts to mask and disrupt the seasonality and dependence on the astronomical sources.

1. Introduction

The main source of cosmic dust into Earth's atmosphere is from a sporadic meteor background not thought to be associated with meteor showers (Janches et al., 2009; Jones & Brown, 1993). Current estimates for the global amount of cosmic dust input range from 22 to 32 t day^{-1} (Carrillo-Sánchez, Bones, et al., 2020; Carrillo-Sánchez, Gómez-Martín, et al., 2020; Dunker et al., 2013; Hervig et al., 2022), and the bulk of this input comprises of meteoroid particles with diameters between 100 and 1,000 μm and entry velocities between 11 and 72 km s^{-1}. Upon interaction with ambient air molecules within the mesosphere and lower thermosphere region (MLT, 75–110 km) (McKinley, 1961; Öpik, 1958; Plane, 2003), these particles heat up, ablate, and produce plasma trails detectable by ground-based meteor radars (Chau et al., 2021; De Wit et al., 2014; Fritts et al., 2010; Jacobi et al., 2007; A. Liu et al., 2013; Marino et al., 2022; Poulter & Baggaley, 1977; Stober, Janches, et al., 2021, Stober et al., 2023).

The sporadic meteor background is composed of particles typically originating from one of six different astronomical source populations, each traveling from a unique direction relative to the Earth (Campbell-Brown & Jones, 2006; Fentzke & Janches, 2008; Jones & Brown, 1993; Schult et al., 2017). The Helion and Anti-Helion sources largely consist of particles originating from the Jupiter Family Comets (JFCs), characterized by low inclination and relatively slow velocities while traveling either to or from the Sun's relative position (Nesvorný et al., 2010). Modeling work has estimated that the main mass contributor to the sporadic meteor background consists of particles originating from the JFCs (Carrillo-Sánchez, Gómez-Martín, et al., 2020; Nesvorný et al., 2010; Rowan-Robinson & May 2013; Zook, 2001). The two Apex sources primarily comprise of dust particles with much higher relative velocities (∼55 km s^{-1} (Fentzke & Janches, 2008; Schult et al., 2017) and originate from Oort Cloud Comet and Halley Type Comet populations (Nesvorný et al., 2010, 2011; Pokorný et al., 2014). Lastly, the north and south Toroidal sources comprise of meteoroids originating from HTCs approaching Earth at high ecliptic latitudes (Pokorný et al., 2014).

The visibility, and thus the relative contribution to the observed sporadic meteor background, of the six different astronomical source populations vary in both LT and season depending on the geographic latitude of an Earth-based observer (Fentzke et al., 2009; Janches et al., 2004, 2015; Schult et al., 2017). The altitude at which individual meteoroids ablate is determined by factors such as the entry velocity, entry angle, particle mass, and composition, all of which can depend on the contributing astronomical source and its relative visibility. In addition, the atmospheric density profile at a particular geographical location also plays a role in the ablation altitude of individual meteoroids (Carrillo-Sánchez et al., 2016; Dawkins, Stober, Carrillo-Sánchez, et al., 2023; Fentzke & Janches, 2008; Plane et al., 2015; Stober et al., 2012, 2014). As individual meteors enter the meteor radar field of view, the altitude of the observed meteor is determined using interferometric techniques (Hocking et al., 2001). Although individual meteor trails have been used since the 1940s to detect and determine horizontal neutral winds and dynamics within the MLT region, there are still only a relatively limited number of studies, which have examined changes in the altitude at which the bulk of detected meteoroids ablate, and to what extent these can be related to atmospheric dynamical variability on various timescales. For example, Clemesha and Batista (2006) examined the centroid of meteoroid altitude distributions for five years of data from the Cachoeira Paulista meteor radar in Brazil at ∼23°S and found evidence of long-term linear changes across this short time period. Lima et al. (2015) later examined data from the same station across solar cycle 23 (1999–2008) and looked for changes in meteor echo height variations over this period. After removing any signal associated with the 11-year solar cycle, they found a linear trend of the meteor echo height of −38 m year^{-1} (i.e., a decrease in altitude), which they interpreted as being caused by a long-term reduction in air density in the upper atmosphere associated with increasing greenhouse gases.

A recent study by Dawkins, Stober, Carrillo-Sánchez, et al. (2023) utilized extensive data records from 12 independent meteor radar stations, representing a diverse range of geographic latitudes and looked for changes associated with both the 11-year solar cycle and those associated with long-term anthropogenic climate change. The authors found long-term linear decreases in the peak altitude of the individual meteor altitude distributions at

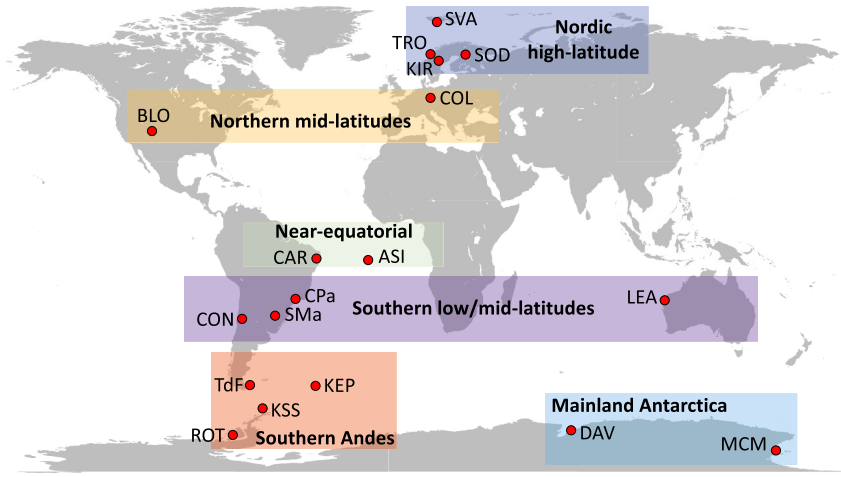

Figure 1. Geographic coverage provided by the 18 meteor radar data sets used in this study clustered into geographic regions (Nordic high-latitude, Northern mid-latitudes, Near-equatorial, Southern low/mid-latitudes, Southern Andes, and Mainland Antarctica).

all latitudes varying between −10.97 and −817.95 m decade^{-1}, which was consistent with a hydrostatic cooling and contracting of the middle and upper atmosphere due to increase in anthropogenic greenhouse gas emissions. They found mixed responses of the meteor peak ablation altitudes with the 11-year solar cycle dependent on the latitude of the meteor radar. At low- and middle-latitudes, they found a positive correlation whereby the meteor peak ablation altitudes increased in height during solar maximum and decreased/lowered during solar minimum as a result of changes in the exposure and absorption of solar extreme ultraviolet, which either heated and caused atmospheric expansion or cooled and caused contraction. However, at high latitudes, they found that the meteor peak altitudes were anticorrelated with the 11-year solar cycle. The latitude differences in the sign and magnitude of the response were thought to be a result of a strong atmospheric dynamics influence that varied by latitude. They found that the behavior of the three meteor radar stations located within the Southern Andes region (Tierra del Fuego, King Sejong Station, and Rothera) differed from other stations at equivalent latitudes. They posited that this could suggest a strong role of atmospheric dynamics in influencing peak altitudes as this region is a known atmospheric gravity wave hotspot (Becker & Vadas, 2018; De Wit et al., 2017; Stober, Janches, et al., 2021; Vadas & Becker, 2018; Vadas et al., 2018).

Although there is evidence that atmospheric variability can result in changes to meteor altitude distributions on multiyear timescales (i.e., as in Dawkins, Stober, Carrillo-Sánchez, et al., 2023; Stober et al., 2014), it is not clear to what extent atmospheric variability may influence these meteor altitudes on shorter timescales (both diurnal and seasonal) and whether this varies by geographic location. In this work, we analyze individual meteor altitude measurements from 18 different meteor radar stations obtained from a diverse range of latitudes to assess whether there is variability on such timescales that differs from that purely expected due to variation in astronomical dust source populations, and whether there is a latitude basis for this.

2. Materials and Methods

Meteor altitude observations were obtained from 18 different meteor radar stations at a broad variety of latitudes; the geographic location of each of these stations is shown in Figure 1, whereas the station name, three-letter given acronym, latitude (°N), longitude (°E), station time zone (UTC), radar operating frequency (MHz), and period of observations from each of the stations is summarized in Table 1. These stations consist of a cluster in the Nordic high-latitude sector, including Svalbard (SVA), Tromsø (TRO), Kiruna (KIR), and Sodankylä (SOD), the Northern mid-latitudes, including Collm (COL) and Bear Lake Observatory (BLO), and the Near-equatorial cluster, which includes São João do Cariri (CAR) and Ascension Island (ASI). The Southern low/mid-latitude cluster includes Learmonth (LEA), Cachoeira Paulista (CPa), Santa Maria (SMa), and the CONDOR network (CON, Chilean Observation Network De meteOr Radars). CONDOR comprises three separate radars, Andes Lidar Observatory (ALO), Southern Cross Observatory (SCO), and Las Campanas Observatory (LCO), but in this

Table 1
Latitude, Longitude, Longitudinal Time Zone, Operating Frequency, and Approximate Data Coverage of the 18 Meteor Radar Stations Used in This Work

Sector	Station	Latitude (°N)	Longitude (°E)	UTC (hour)	Frequency (MHz)	Included date range	Approx. Years
Nordic high-latitude	Svalbard (SVA)	78.2	16.0	+1	31.0	01/2002–06/2022	20
	Tromsø (TRO)	69.6	19.2	+1	30.3	12/2003–04/2022	18
	Kiruna (KIR)	67.5	20.3	+1	32.5	08/1999–04/2022	22
	Sodankylä (SOD)	67.4	26.6	+2	36.9	10/2008–04/2022	13
Northern mid-latitudes	Collm (COL)	51.3	13.0	+1	32.6	07/2004–03/2022	18
	Bear Lake Observatory (BLO)	42.0	−111.3	−7	32.5	03/2008–01/2014, 08/2016–12/2017, 08/2018–05/2021	10
Near-equatorial	São João do Cariri (CAR)	−7.4	−36.5	−2	35.24	05/2004–03/2009, 06/2018–12/2021	10
	Ascension Island (ASI)	−7.9	−14.4	−1	43.5	05/2001–04/2007, 02/2009–08/2012	10
Southern low/ mid-latitudes	Learmonth (LEA)	−22.2	114.1	+8	35.24	01/2001–04/2002, 01/2005–12/2006	4
	Cachoeira Paulista (CPa)	−22.2	−45.0	−3	35.24	03/1999–03/2008, 06/2012–12/2021	20
	Santa Maria (SMa)	−29.7	−53.8	−4	35.24	05/2004–04/2012	8
	CONDOR (CON)	−30.3	−70.7	−5	35.1	06/2019–01/2024	5
Southern Andes	Tierra del Fuego (TdF)	−53.8	−67.8	−5	32.6	01/2008–01/2022	15
	King Edward Point (KEP)	−54.2	−36.0	−2	32.5	02/2016–11/2020	5
	King Sejong Station (KSS)	−62.0	−58.0	−4	33.2	03/2007–06/2022	16
	Rothera (ROT)	−67.3	−68.1	−5	32.5	03/2005–04/2022	18
Mainland Antarctica (MA)	Davis (DAV)	−68.6	78.0	+5	33.2	01/2005–09/2021	17
	McMurdo (MCM)	−77.5	165.0	+11	36.17	03/2018–07/2022	4

work, these data sets are combined due to the relative geographic proximity of the respective stations. Finally, the Southern Andes sector comprises of Tierra del Fuego (TdF), King Edward Point (KEP), King Sejong Station (KSS), and Rothera (ROT), and we include both Davis (DAV) and McMurdo (MCM) to form the Mainland Antarctica (MA) cluster. Each of these meteor radar data sets were chosen as they represent near-global coverage, and the majority comprise long-term data sets (10+ years, see Table 1) with most currently still operational. The operating frequencies of the meteor radars included in this work (Table 1) are sufficiently similar which results in individual meteoroids of the same size (diameter) distribution being observed. This also ensures that any differences in the altitude distribution are dominated by astronomical or atmospheric effects rather than observational bias due to the utilization of different frequencies (Olsson-Steel & Elford, 1987).

To find the peak meteor altitude, we form a histogram of all individual meteor altitudes between 83 and 103 km (across the MLT region) in 0.5 km altitude and 1-hr LT bins for each day of the year (DOY) at each location inclusive of data from all years. A flexible nonparametric kernel smoothing curve is fitted to the histogram to determine the most common observed altitude, defined as "peak altitude," at the curve maximum (shown in Figure 2). From this, we obtain a multiyear peak altitude variation as a function of LT and DOY for each meteor radar station location. We consider each LT and DOY bin only if it comprises at least 150 individual observations to avoid low sample size bias.

3. Results and Discussion

Figure 3 presents the variation of peak meteor altitude as a function of LT and DOY for each of the 18 locations organized by geographic cluster (Row 1: Nordic high-latitude cluster, Row 2: Northern mid-latitudes, Row 3: Near-equatorial, Row 4: Southern low/mid-latitudes, Row 5: Southern Andes, and Row 6: Mainland Antarctica (MA)). All data represent an average across all available years for each station. Data are shown for each LT and DOY bin only if it comprises at least 150 individual observations inclusive of all years. There is latitude variation in both seasonality and LT, with the smallest seasonal variation in peak altitudes at low- and mid-latitude locations (Figure 3, panels e–l) and more pronounced seasonal variation at higher latitudes toward the poles. For the Nordic high-latitude sector locations (panels a–d), there is an apparent semiannual seasonality with higher peak

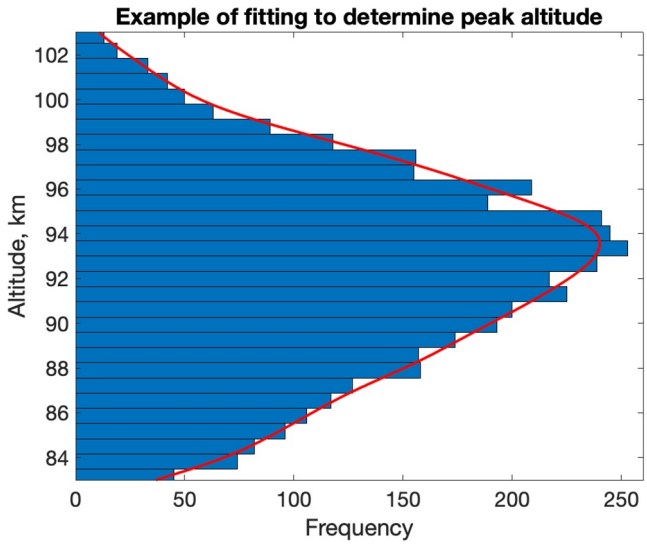

Figure 2. Example of fitting method used to determine peak meteor altitude for each day-of-year (DOY) and 1-hr local time (LT) bin. A nonparametric kernel smoothing flexible fit is applied to a histogram of all individual multiyear meteor observations made for each given 1-hr LT bin for each DOY at a specific location. The altitude at the maximum of the fit is recorded. In this example, a histogram is formed of all individual multiyear meteor observations made at Svalbard (SVA) for DOY 275 and the 08:00 LT bin before a flexible fit is applied to determine the peak meteor altitude as 93.63 km.

altitudes occurring during spring and autumn, and lower peak altitudes in summer and winter. For the MA sector, an annual variation in the peak altitude is seen with the lowest altitudes during the hemispheric wintertime (DOY 150–250). There is some evidence of hemispheric mirroring among all stations, with slightly elevated peak altitudes occurring during hemispheric autumn in most locations. The most pronounced LT variation is found at low- and mid-latitudes and is typically centered around 06:00 LT. At high latitudes, this LT variation is less pronounced. At low- and mid-latitude stations (panels e–l), there is a clear bimodal LT variation in the peak latitudes. However, the Southern Andes stations (panels m–p) exhibit a more complex variation in peak altitude. Although both TdF and KEP (panels m–n) exhibit a very weak bimodal distribution in peak altitude close to day 90 that weakly mirrors that of the Northern Hemisphere (NH) latitude stations, COL and BLO (panels e–f), around day 270, this is not seen in the more poleward KSS and ROT station data. However, common to each of the Southern Andes stations is an apparent LT peak altitude maximum, which drifts by season.

In Figure 4, we present the elevation angle (°) of the combined astronomical sources as a function of DOY and LT for each of the 18 locations organized by geographic cluster. This is calculated taking the instantaneous elevation of the center of each source and weighted according to the source strength given by Fentzke and Janches (2008): north and south Apexes (20% total), Helion (35%), Anti-Helion (35%), and either the north or south Toroidal (depending on hemisphere, 10%).

There is a considerable seasonal and LT variation in the combined astronomical sources; this is because the weighted elevation angle of the meteor source population trajectories varies and is highly dependent on latitude and season (Fentzke & Janches, 2008; Janches et al., 2008; Schult et al., 2017; Sparks & Janches, 2009). At higher latitudes and during certain seasons, some of the sources may be so low in the sky that the Earth will mask part of the incoming meteoroid flux. Thus, the seasonal variability in meteoroid flux is expected to be the largest at high latitudes. In contrast, there is no significant change in the elevation angles at low latitudes, and the weighted elevation angle remains largely consistent across seasons. Due to the observing geometry, the elevation angles during hemispheric spring are typically a lot more shallow than those in the hemispheric autumn for most astronomical sources and at all latitudes (Sparks & Janches, 2009). At high latitudes, this is most pronounced as the Apex sources, which are dominated by higher speed particles, typically have very high entry elevation angles during autumn and are thus more readily observed (Fentzke et al., 2009). At lower latitudes, there is less seasonal variation in the contribution of the Apex sources. Instead, the bimodal altitude variation seen in the majority of low- and mid-latitudes is largely due to the changing observing geometry of the Helion and Anti-Helion sources (Fentzke et al., 2009 and references therein).

Although there is very little seasonal difference in the combined astronomical source elevation angles at low-latitudes, the opposite is true in terms of diurnal variation. It is at these low-latitudes where there is the most pronounced diurnal variation in elevation angle; the respective sources may be high in the local sky during part of the day but then be below the observing horizon at other times. For higher latitudes, this diurnal variation in elevation angle is not as pronounced within a given season. Sparks and Janches (2009) found that, for most sources, the highest elevation angles occur between local midnight and 07:00 LT whereas the minimum occurs at approximately 19:00 LT. This morning maximum is consistent with when the dominant astronomical sources are highest in the local sky (Sparks & Janches, 2009).

For the majority of meteor radar station locations, there is a qualitative agreement between the seasonal and LT altitude variation in the visibility of the combined astronomical source and that of the peak meteor variation; higher meteor ablation altitudes typically coincide with higher elevation angles of the combined source. This is particularly true for DOY 250–320 within the NH locations and to a lesser extent in DOY 50–150 in the Southern Hemisphere (SH) locations (Figure 3). This is consistent with the hemispheric autumn maximum in the weighted elevation angle of the astronomical sources; a higher elevation angle will result in faster velocities of the incoming

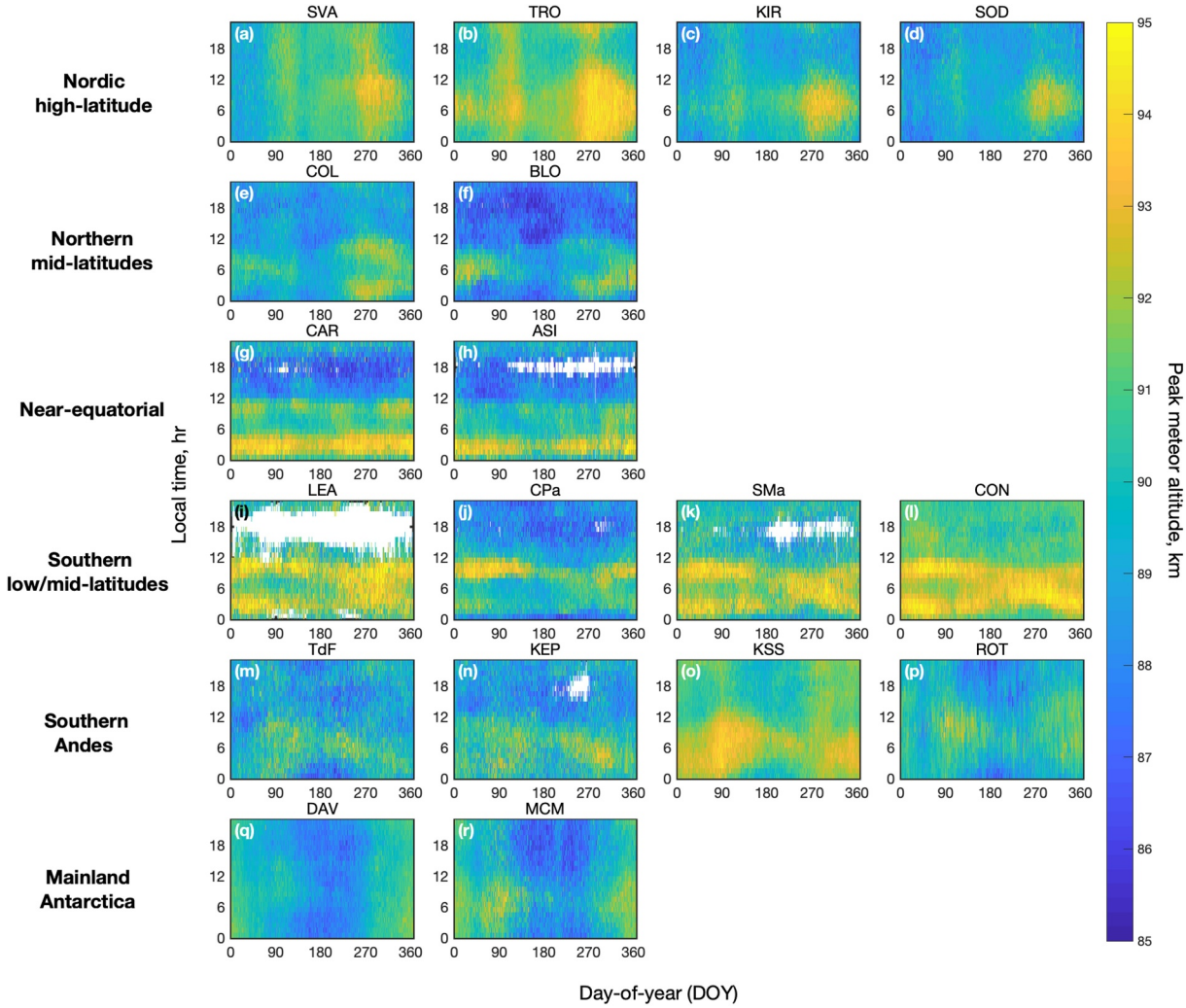

Figure 3. Variation in peak meteor altitude as a function of local time and day-of-year (DOY) for each of the 18 locations: (a) SVA, (b), TRO, (c) KIR, (d) SOD, (e) COL, (f), BLO, (g) CAR, (h) ASI, (i) LEA, (j) CPa, (k) SMa, (l) CON, (m) TdF, (n) KEP, (o) KSS, (p) ROT, (q) DAV, and (r) MCM. Each row represents a different geographic sector: (Row 1) Nordic high-latitude, (Row 2) Northern mid-latitudes, (Row 3) Near-equatorial, (Row 4), Southern low/mid-latitudes, (Row 5) Southern Andes, and (Row 6) Mainland Antarctica. The color scale denotes the peak meteor altitude (units: km).

meteoroids, and they will heat up and ablate (and be detectable by meteor radars) at higher altitudes in the Earth's atmosphere. For the majority of locations, a diurnal maximum centered around 06:00 LT can also be seen, which matches the diurnal maximum in the elevation angle of the combined astronomical source. The pronounced daily bimodal altitude variation seen throughout all DOYs at the majority of the low- and mid-latitude stations (COL, BLO, CAR, ASI, LEA, CPa, SMa, and ALO, and to a much lesser extent, TdF and KEP around DOY 90) is likely a result of the sharp diurnal variation of the combined astronomical source and the relative contributions of the Helion and Anti-Helion sources (Fentzke et al., 2009) to the weighted elevation angle.

However, there is some seasonal and LT altitude variation apparent at a number of locations, which cannot be explained solely by variation in the weighted elevation angle of the combined astronomical sources. These include both the spring peak altitude maxima within the Nordic high-latitude region stations as well as the enhanced peak altitudes in the Southern Andes sector stations during DOY 200–300 or within the MA sector stations prior to DOY 50 and after DOY 250. This indicates some other factor is impacting or masking the seasonal and LT variation than would be expected by changes in the visibility of the combined astronomical source given by the elevation angles alone.

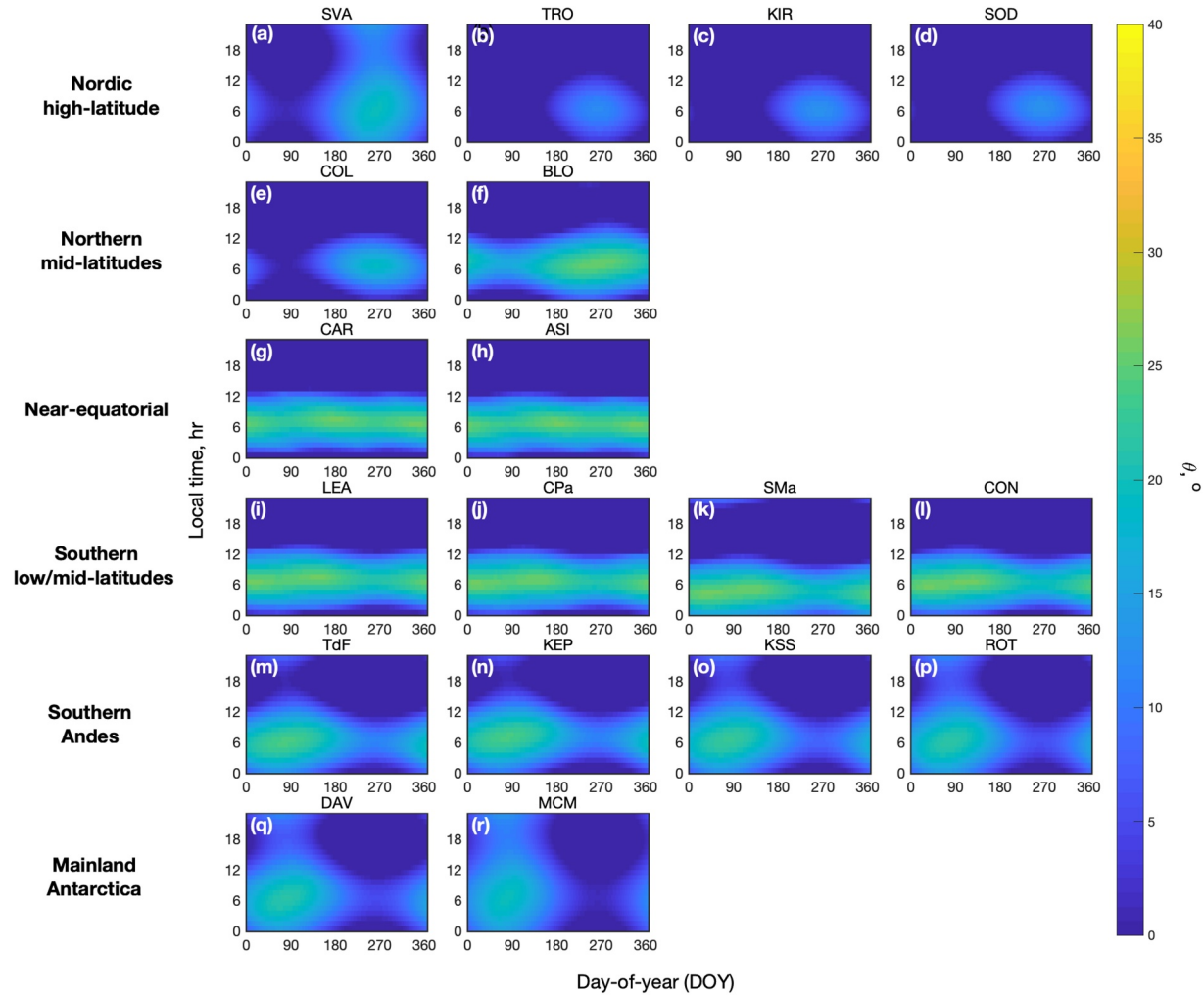

Figure 4. Variation in the weighted elevation angle, theta, of the combined astronomical sources as a function of local time and day-of-year (DOY) for each of the 18 locations: (a) SVA, (b) TRO, (c) KIR, (d) SOD, (e) COL, (f) BLO, (g) CAR, (h) ASI, (i) LEA, (j) CPa, (k) SMa, (l) CON, (m) TdF, (n) KEP, (o) KSS, (p) ROT, (q) DAV, and (r) MCM. Each row represents a different geographic sector: (Row 1) Nordic high-latitude, (Row 2) Northern mid-latitudes, (Row 3) Near-equatorial, (Row 4), Southern low/mid-latitudes, (Row 5) Southern Andes, and (Row 6) Mainland Antarctica. The color scale denotes the weighted elevation angle (units: °).

To further investigate the nature of these seasonal and LT altitude variations demonstrated in Figure 3, we present Figure 5, which focuses on the residual seasonal variation at four different local times (00:00 LT, 06:00 LT, 12:00 LT, and 18:00 LT). This residual seasonal variation is determined by subtracting the mean peak altitude across the full-time series for a given 1-hr LT bin for each station. Each row represents stations grouped into one of the six different geographic sectors. Data for all SH locations are shifted by ∼180 days so as to align NH summer with SH summer, etc. One can still see that the residual seasonal variation increases toward the poles irrespective of LT. There are also differences in the seasonal response for different LTs, indicating there is a real LT variation in the majority of locations. There is a very clear consistency in the semiannual variation in peak altitude seen across the Nordic high-latitude locations (panels a–d) with an increase in peak altitude during spring and autumn, near-zero variation during summer, and a wintertime minimum. There is also a consistent response in the Northern mid-latitude locations with a small increase in peak altitude during spring and a larger increase during autumn for some of the LTs presented. Although true for COL, this is not as pronounced for BLO, which likely reflects that the BLO data set comprises fewer years of data (∼10 years of nonconsecutive coverage) than that of COL (∼18 years) and thus likely exhibits increased shorter-term variability during certain LTs and DOYs where data coverage is less uniform.

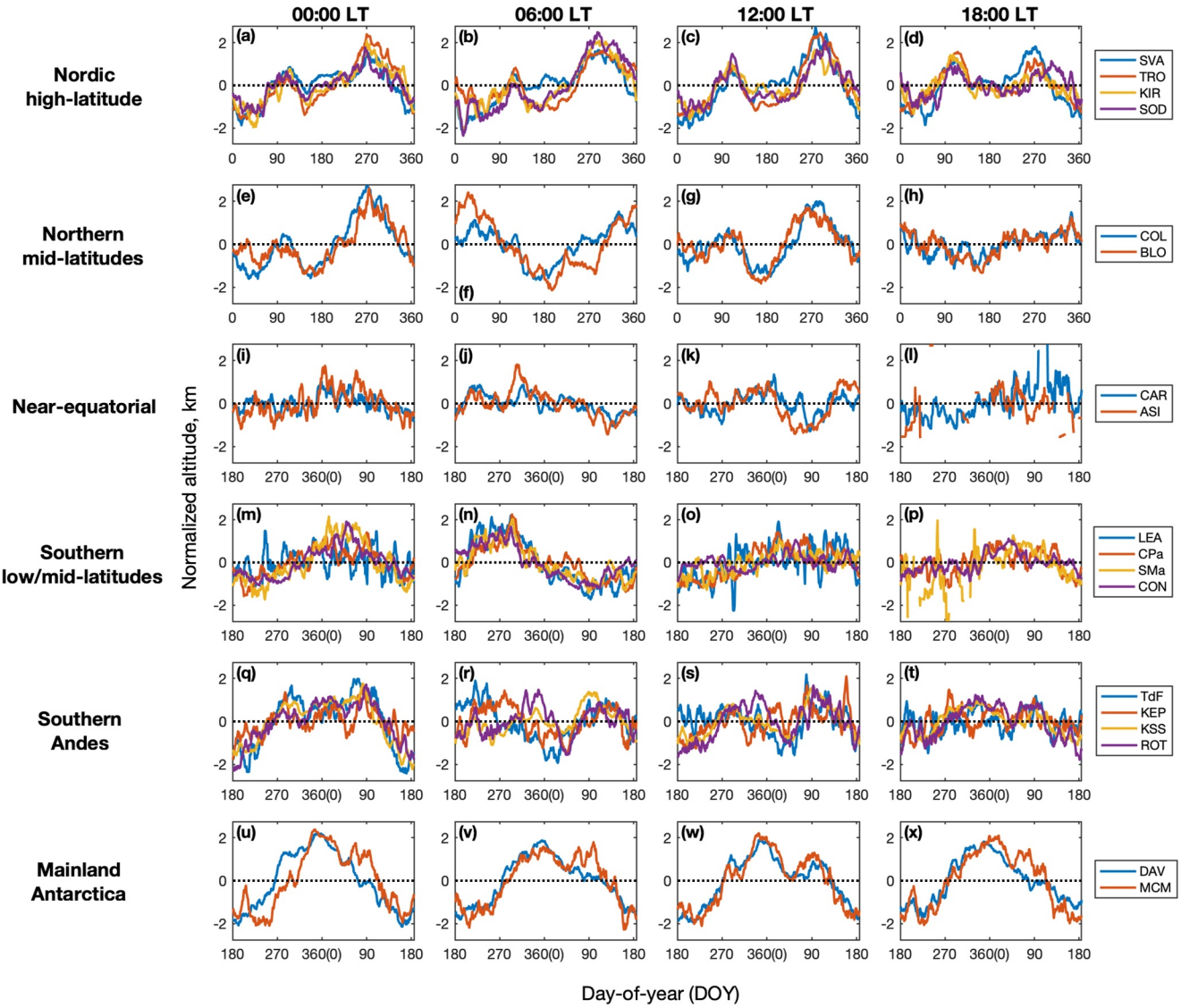

Figure 5. Residual seasonal variation in peak altitude for each location at four different local times (different columns corresponding to 00:00 LT, 06:00 LT, 12:00 LT, and 18:00 LT). Each row represents a different geographic sector: (Row 1) Nordic high-latitude, (Row 2) Northern mid-latitude, (Row 3) Near-equatorial, (Row 4), Southern low/mid-latitudes, (Row 5) Southern Andes, and (Row 6) Mainland Antarctica. Each panel is a function of both DOY and normalized altitude (units: km). The data for all Southern Hemisphere (SH) locations (Rows 3–6) are shifted by 180 days to allow for easier seasonal comparison (i.e., now the SH winter appears at the same DOY as the NH winter).

In contrast to the largely consistent NH station response, there is a much more varied and complex response among the SH locations. The LT and seasonal variation at the Near-equatorial stations (CAR and ASI, Row 3) is minimal, and it should be noted that there is limited data coverage for ASI at 18:00 LT (panel l). The most pronounced and coherent seasonal variation for the Southern low/mid-latitude stations (LEA, CPa, SMa, CON) occurs at 06:00 LT (panel n) with a hemispheric spring maximum and autumn minimum, but otherwise, there is a minimal LT and seasonal response with some noticeable variation among stations. As with COL and BLO, the difference in data period coverage could explain some of this intra-sector variability; although CPa comprises nearly 20 years of data, LEA, SMa, and CON have much shorter data period lengths at approximately 4, 8, and 5 years, respectively. While the Southern Andes sector stations also exhibit pronounced LT variation, they largely have a more muted seasonal variation overall and the actual response of individual stations is very variable despite the data period lengths for three of the stations, TdF, KSS, and ROT, being substantial (15, 16, and 18 years, respectively). The MA locations (DAV and MCM) show a striking annual variation in peak altitude, which strongly differs from the semiannual response seen at many other locations particularly that of the NH station with

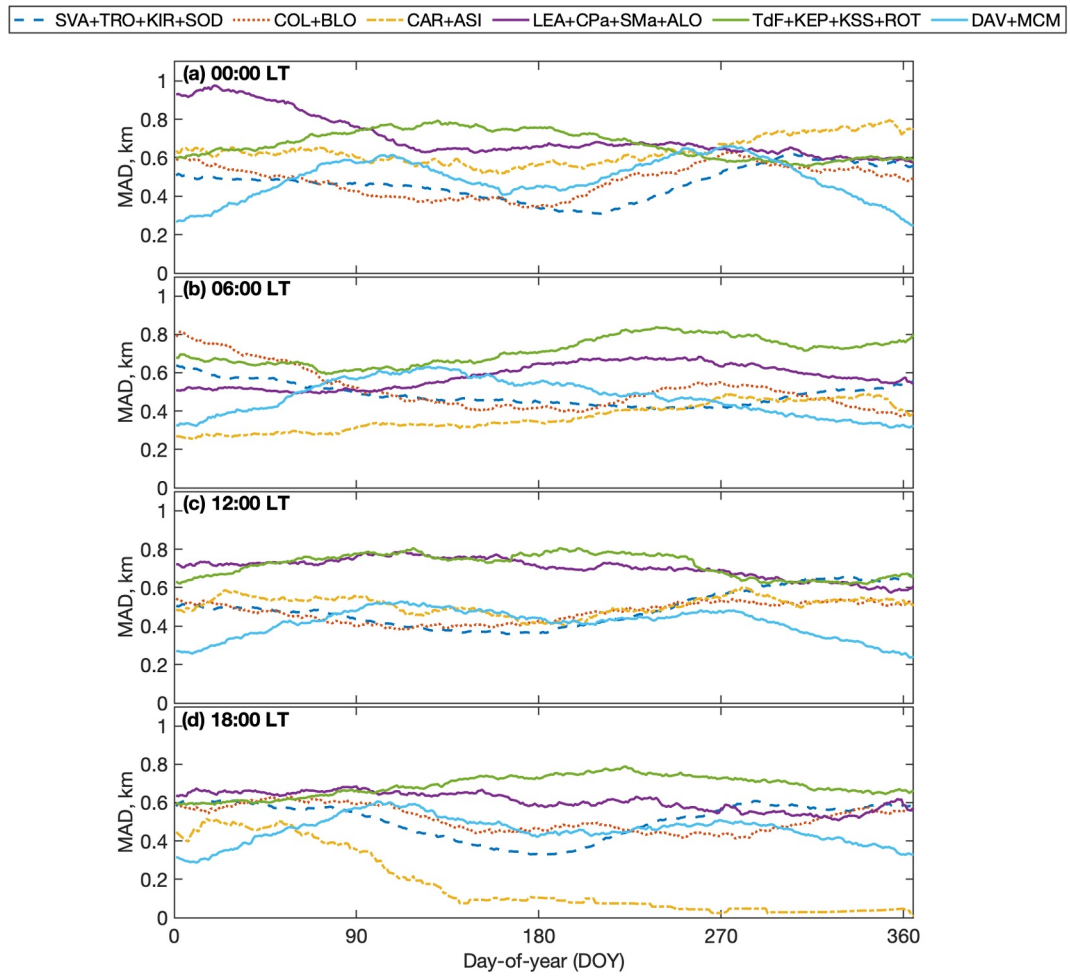

Figure 6. The mean absolute deviation (MAD) of each of the different geographic clusters presented as a function of DOY for four different local times (00:00 LT, 06:00 LT, 12:00 LT, and 18:00 LT). A 90-day moving average smoothing function is applied to the MAD.

the closest equivalent latitude, SVA. Importantly, this distinct annual variation is seen across both MA stations, despite MCM only comprising of ∼4 years of data, compared to the much longer ∼16 years data set of DAV.

If the variation in meteor peak altitude were purely astronomical, a symmetrical seasonal variation would be expected (for a given LT) between the NH and SH locations, yet this is clearly not the case. This is illustrated by the notable differences between the seasonal variation of the NH and SH station locations.

It is clear that for some geographic sectors, differences exist in the LT and seasonal peak altitude residuals between stations. To further examine this, Figure 6 depicts the mean absolute deviation (MAD) between the seasonal peak altitude residuals among the different stations within each geographic sector for the four different local times (00:00 LT, 06:00 LT, 12:00 LT, 18:00 LT). The MAD is estimated as $1/n\sum_{i=1}^{n}|x_i - \bar{x}|$, and describes the average distance between a sample (x_i) and the mean $(\bar{x})$, providing an estimate of variability while taking into account sample size (n). A 90-day moving average smoothing function is applied to minimize the impact of shorter-term (day-to-day) variation. The MAD varies between different local times and DOYs. For most DOYs, the Nordic high-latitude, Northern mid-latitude, Near-equatorial, and MA clusters exhibit the least variation between their different respective stations, while the Southern low/mid-latitude and Southern Andes clusters exhibit substantially more variation. The MAD for the Southern Andes cluster is high but is very consistent as a function of both LT and DOY (i.e., the different stations are consistently different in their responses). Meanwhile, the MAD for the Southern low/mid-latitude cluster is also high but is more seasonally variable (i.e., during certain LTs and seasons these stations exhibit more similar peak altitudes vs. other times in which there is divergence and

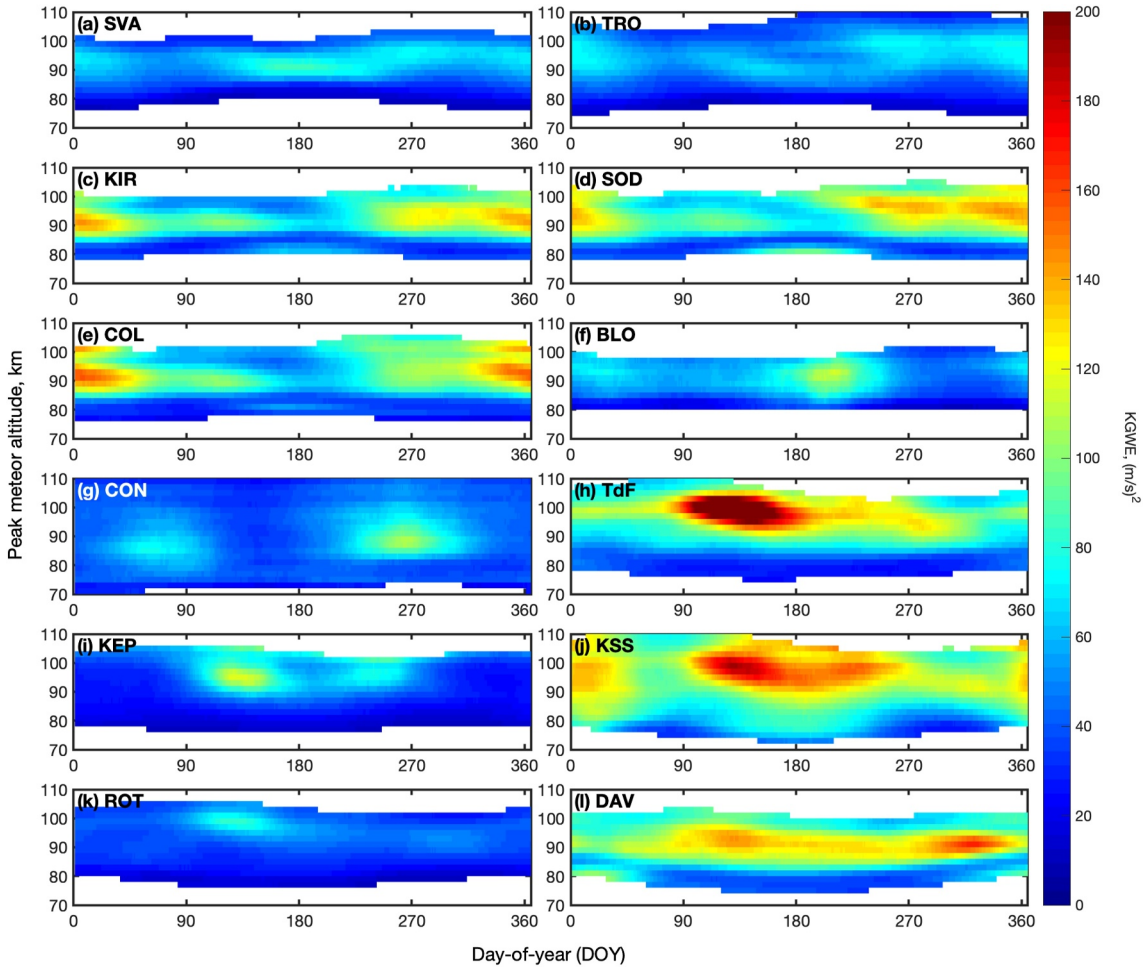

Figure 7. Kinetic gravity wave energy as a function of time of year and altitude (km) for 12 locations: (a) SVA, (b) TRO, (c) KIR, (d) SOD, (e) COL, (f) BLO, (g) CON (Andes Lidar Observatory only), (h) TdF, (i) KEP, (j) KSS, (k) ROT, and (l) DAV.

more prominent differences). The Southern Andes sector is a known highly active gravity wave (GW) hotspot (Becker & Vadas, 2018; Fritts et al., 2010; Stober, Janches, et al., 2021; Vadas et al., 2018); the consistently high MAD for this cluster in Figure 6 could be indicative of a strong atmospheric variability reflective of this, impacting the meteor peak altitudes, in addition to the variability given by the varying visibility of the astronomical source.

From linear theory (Fritts & Alexander, 2003), we can estimate that medium frequency GWs can induce atmospheric neutral density changes of the order of a few percent (Stober et al., 2022). Thus, enhanced GW activity should manifest in increased neutral density variability, which may affect the altitudes at which meteors are detected. In Figure 7, we present the kinetic gravity wave energy (KGWE) derived from the hourly meteor wind after subtracting the large-scale mean flow and the diurnal, semidiurnal, and terdiurnal tides using the adaptive spectral filter with vertical regularization (ASF2D) (Baumgarten & Stober, 2019; Stober et al., 2020), which we utilize here as a proxy for GW activity (Stober, Janches, et al., 2021). The KGWE is estimated as KGWE = 1/2 $(u'^2 + v'^2)$ where u' and v' are the GW perturbation components of the zonal and meridional wind velocity field, respectively. The ASF2D is most sensitive to GW periods longer than 2 hr and horizontal wavelengths larger than 300 km, which can sometimes be associated with secondary wave generation due to local body forces at the stratosphere caused by breaking mountain waves (Becker & Vadas, 2018; Vadas & Becker, 2018; Vadas et al., 2018). Shown are the KGWE as a function of time of year and altitude for six locations in the NH (SVA, TRO, KIR, SOD, COL, and BLO) and six locations in the SH (CON, TdF, KEP, KSS, ROT, and DAV). In general, one can see that the KGWE across each of the six NH locations is largely very consistent with one another

in terms of both altitude and seasonal variation. There is enhanced KGWE activity during mid-late spring, autumn, and winter across all six NH stations and enhanced KGWE activity during summertime at the higher latitude locations. In contrast, the seasonal and altitude-related KGWE activity for each of the six SH station locations varies significantly not only from one another but also compared to each of the NH locations. This is most clearly seen when comparing the responses for the Southern Andes stations. TdF and KSS, which are located close to the Drake Passage, exhibit the most pronounced deviations from all other stations. This is likely related to their location close to the Southern Andes and Antarctic Peninsula, both strong sources of primary orographic GWs (Becker & Vadas, 2018; Vadas & Becker, 2018), as well as their proximity to the stratospheric wind maximum on the northernmost edge of the polar vortex (~50°S). This polar jet wind maximum, which can reach up to 130 ms^{-1} (Stober, Janches, et al., 2021), essentially becomes a source of GWs itself due to jet instabilities as well as enabling larger scale orographic waves to propagate to higher altitudes without becoming convectively unstable, thus preventing GW saturation and enabling GW propagation to higher altitudes. Each of these results in increased KGWE activity during the hemispheric winter at both TdF and KSS. Although not captured by the KGWE (which is sensitive to GWs with horizontal scales greater than 300 km), it is worth noting that the polar vortex can also act as an efficient filter for vertically propagating GWs with much smaller horizontal wavelengths (less than 30 km). Such small-scale wave are likely to be reflected or to tunnel through the evanescent region created by the stratospheric winds (Heale & Snively, 2015; Mixa et al., 2021).

The relative location of each of the Southern Andes stations to the primary orographic GW sources and the stratospheric polar jet maximum appears to influence the KGWE exhibited. The wintertime KGWE at TdF exceeds that of KSS, most likely as a result of the Andes main ridge being a much stronger source of orographic GWs than the Antarctic Peninsula. In addition, TdF is located closer to the latitude of the polar vortex wind maximum, which likely further contributes to the much larger KGWE exhibited here than at KSS and other stations. The importance of mountain waves generated by the Andes main ridge becomes more clear when comparing TdF and KEP; although both are located at the same southern latitude (and thus are likely similarly influenced by the polar jet maximum), they reflect substantial differences in the GW activity, which results from their respective distances from the prominent orographic GW sources. The reduced KGWE at ROT provides an additional example of the relative impacts of proximity to orographic GW sources and the polar jet maximum to the KGWE; although ROT is located far inside the polar vortex and is thus further away from the latitude of the stratospheric wind maximum, it is also located further from the orographic GW sources that most heavily influence TdF and KSS in the Drake passage. These results highlight that the GW activity is less coherent across different locations within the SH even for those within the same geographic region, which further supports the suggestion that the variability we see within the SH meteor station altitude data sets is more dominated by these dynamical effects than by astronomical source visibility compared to the NH locations.

Focusing on the four stations within the Southern Andes cluster (TdF, KEP, KSS and ROT), we can simulate the peak altitude variation that would be expected due to variations in the weighted elevation angle of the particle source alone (i.e., excluding any atmospheric dynamical effects). We use the simulated mass profiles from the University of Leeds Chemical Ablation model (CABMOD) (Vondrak et al., 2008) for a meteoroid particle of a fixed initial mass (200 μg) and velocity (31 km s^{-1}) at a latitude of 60°S. Figure 8 presents the particle mass profiles for four different months (March, June, September, and December) and for two example elevation angles relevant to the Southern Andes stations (5° and 25° as demonstrated in Figure 5 (panels (h), (j), (l), and (n)). As can be seen, the particle loses mass as it descends through the Earth's atmosphere due to ablation. However, the mass profiles differ between different months and for different elevation angles; particles during June (Figure 8, panel c) reach lower altitudes before losing all mass compared to the other months. Particles with lower entry angles also survive longer in the atmosphere irrespective of month.

We determine the peak altitude as the altitude at which 80% of the original particle mass has ablated (Dawkins, Stober, Carrillo-Sánchez, et al., 2023), and this is denoted and labeled in panels (b)–(e) by either a filled triangle or filled circle for entry angles of either 5° and 25°, respectively. In Figure 9, we demonstrate that the observed meteor peak altitude variation cannot be reproduced by only considering variations in the weighted elevation angle of the astronomical source population. For the left-hand side column panels, we show the simulated altitude using CABMOD mass profiles, whereas the observed peak altitudes are shown in the right-hand side column. For all four locations, the observed LT and seasonal variation are stronger and much more complex than that simply attributable to variation in the astronomical source, and instead better mirrors the KGWE activity presented in

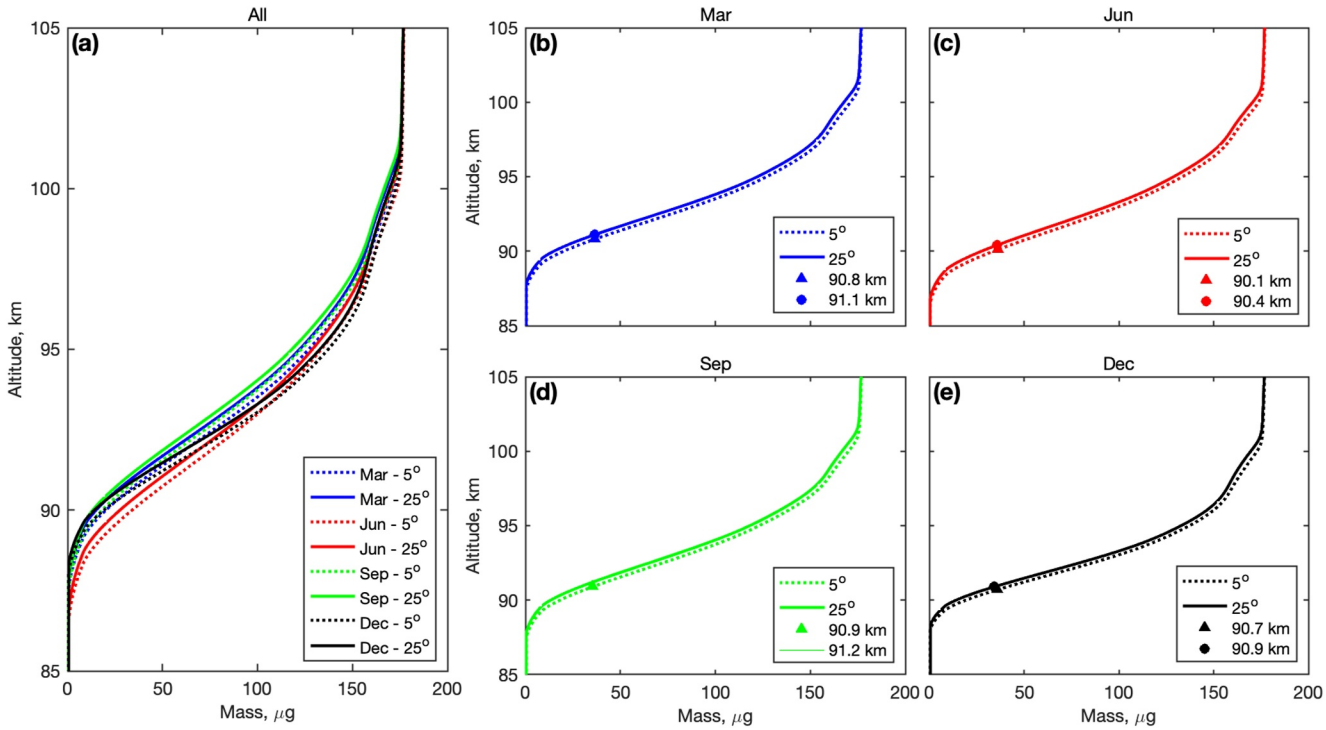

Figure 8. Example vertical mass profiles from CABMOD for a meteoric particle with a fixed initial mass (178 μg) and velocity (31 kms^{-1}) at a latitude of 60°S. Panel (a) presents mass profiles (units: μg) as a function of altitude (km) for four different months (Mar, Jun, Sep, and Dec), with meteoric particle entry of either 5° or 25° (entry angles relevant to the Southern Andes stations seen in Figure 5). Panels (b)–(e) depict the vertical mass profiles for each of the 4 months. The altitude at which 80% of the initial mass is lost is indicated by the filled triangle or filled circle for entry angles of 5° and 25°, respectively.

Figure 7. This suggests that the LT and seasonal variation in the peak altitude are instead dominated by atmospheric dynamics, at larger scales by planetary waves (Stober et al., 2012) and tides and at shorter periods and locally by GW activity for these locations. This atmospheric variation masks and disrupts any variation that would be expected due to variation in the astronomical source alone. Although our analysis indicates a clear LT dependency of the peak altitude, atmospheric tides are only a minor contributor to this variability. Atmospheric tides often have a vertical wavelength that is comparable to the width of the meteor layer (Stober, Brown, et al., 2021; Stober, Janches, et al., 2021; Stober, Kuchar, et al., 2021) and, thus, warm and cold phases of the tides cancel each other out resulting in a suppressed response of our method to this type of variability. Furthermore, we mitigated a potential contamination due to nonmigrating tides by removing the longitudinal dependence and presenting our analysis in LT. The contribution of the migrating tide, assuming a vertical wavelength much larger than the meteor layer, was estimated to only result in a change of 5% of the scale height (corresponding to approximately 10 K tidal amplitude) or to a variability of 300 m in the meteor peak altitude.

4. Summary and Conclusions

Meteoroids ablate in the Earth's MLT region (75–110 km), and the resulting plasma trails can be detected by ground-based meteor radars. The altitude at which an individual meteoroid ablates depends on the mass, velocity, composition, and entry angle of the particle as well as on atmospheric density (Janches et al., 2017; Vondrak et al., 2008). The mass, velocity, composition, and entry angle of the particle depend on the astronomical source population that the individual meteoroid may originate from and thus should reflect the diurnal, seasonal, and latitudinal variation of the specific astronomical source population. However, on longer-term timescales (decadal, 11-year solar cycle), the mean (peak) meteor ablation altitudes primarily reflect long-term atmospheric density changes (Clemesha & Batista, 2006; Dawkins, Stober, Carrillo-Sánchez, et al., 2023; Lima et al., 2015; Stober et al., 2014). Currently, it is not clear to what extent atmospheric variation influences the peak meteor altitudes on shorter diurnal and seasonal timescales, whether any altitude variation primarily reflects that of the astronomical source populations, and whether there is any latitude basis to this atmospheric versus astronomical dependence.

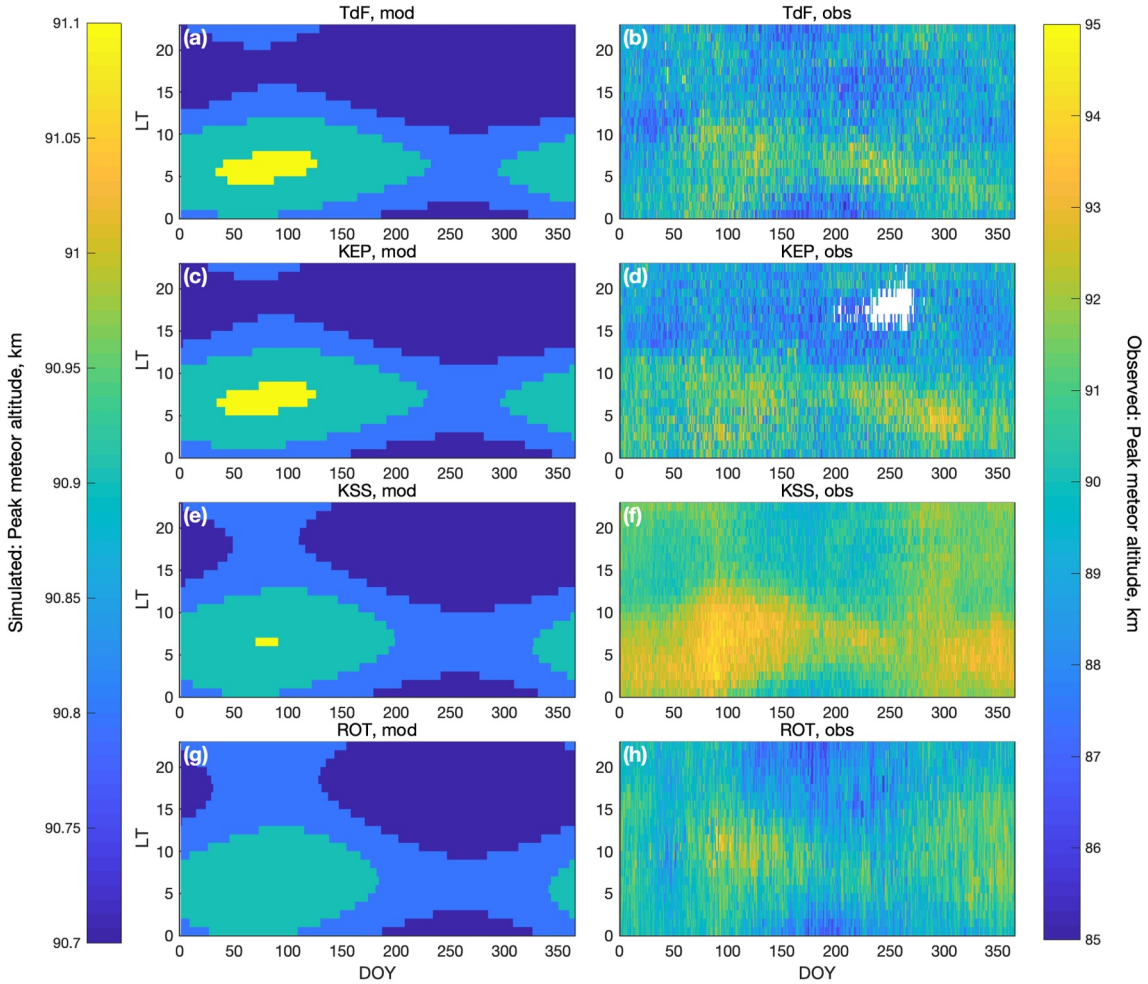

Figure 9. Simulated and observed meteor peak altitudes (km) as a function of DOY and local time for each of the four Southern Andes station locations (TdF, KEP, KSS, and ROT).

In this work, the short-term (diurnal and seasonal) variation in the meteor peak altitudes was assessed as a function of both LT and DOY for 18 meteor radar stations, representing six different geographic regions; Nordic high-latitude, Northern mid-latitude, Near-equatorial, Southern low/mid-latitude, Southern Andes, and Mainland Antarctica. We found evidence that, in less active GW regions, the visibility of astronomical sources plays a more dominant role in the variation in the meteor peak altitude. However, we noted a divergence in the meteor peak altitude variation from that expected due to astronomical source variation alone at all locations, which indicates an additional dependence on atmospheric variability.

This dependence of the peak altitude on the atmospheric variability varies by geographic sector. Typically stations within the same geographic sector exhibited very similar LT and seasonal variation to one another. In particular, we found a very consistent LT and seasonal response in the peak altitudes of each of the NH locations regardless of latitude. We found a coherent semiannual variation in the peak meteor altitudes across all NH stations with altitude maxima in both spring and autumn. Although the elevated altitudes during autumn are strongly correlated with the astronomical source, the springtime altitude maxima is likely due to the sudden breakup of the polar vortex that occurs during the transition from hemispheric winter to summer and might also be linked to the vertical coupling event of a sudden stratospheric warming, which causes large scale changes in the vertical wind and temperature layering from the stratosphere to the mesosphere (Harvey et al., 2022; Matthias et al., 2021; McCormack et al., 2017; Stober et al., 2012, 2020).

In contrast to this coherent NH response, the response of the LT and seasonal altitude variation in the SH was much more complex and diverse. The two Mainland Antarctica stations, DAV and MCM, both exhibit an annual variation quite distinct from that exhibited by any other station in other geographic regions, including that of SVA which is the most poleward NH location. Although the seasonal variation broadly reflects that of the astronomical source, the lack of a springtime peak altitude maximum as seen at SVA likely reflects atmospheric changes due to a smoother breakup of the SH polar vortex compared to the NH event. The combined lack of the planetary waves within the SH polar region along with a more pronounced ozone depletion creates conditions that result in a more stable and persistent polar vortex (Schoeberl & Newman, 2015). Due to this, sudden stratospheric warming events are much less frequent in the SH and thus the transition from hemispheric winter to summer appears to be less driven by dynamical processes compared to the NH (G. Liu et al., 2022; Stober, Janches, et al., 2021).

Although we typically found stations within the same geographic sector exhibit similar LT and seasonal variation, this was not true for stations within either the Southern low/mid-latitude or Southern Andes sectors, and we found the largest MAD in response between adjacent stations located near the Southern Andes (TdF, KEP, KSS, and ROT). This is likely due to enhanced GW variability across the Andes, which impacts each station differently, and this GW activity appears to mask any diurnal variation and seasonality that would be attributable to variation in the different astronomical source populations alone.

Acronyms

ALO	Andes Lidar Observatory (part of the CONDOR network)
BLO	Bear Lake Observatory
CAR	São João do Cariri
COL	Collm
CPa	Cachoeira Paulista
CEDA	Centre for Environmental Data Analysis
CON	Chilean Observation Network De meteOr Radars (CONDOR). Comprises of the ALO, SCO and LCO meteor radars
DAV	Davis
DEL	Delamere
GW	Gravity Wave
KEP	King Edward Point
KSS	King Sejong Station
KIR	Kiruna
LEA	Learmonth
LCO	Las Campanas Observatory (part of the CONDOR network)
LT	Local Time
MA	Mainland Antarctica
MCM	McMurdo
NH	Northern Hemisphere
ROT	Rothera
SH	Southern Hemisphere
SMa	Santa Maria
SCO	Southern Cross Observatory (part of the CONDOR network)

SOD	Sodankylä
SVA	Svalbard
TdF	Tierra del Fuego
TRO	Tromsø
UTC	Universal Time Coordinated

Data Availability Statement

The analyzed data presented in this manuscript (Figures 3–9) are available at https://doi.org/10.5281/zenodo.12533628 (Dawkins, 2024). The individual meteor radar files used as input for this work can either be made available upon request from individual co-authors or in some cases are already publicly available online. Please contact A. Kozlovsky (alexander.kozlovsky@oulu.fi) for the Nordic Meteor Radar Cluster data (SVA, KIR, TRO, SOD). Request for access to the COL meteor radar data can be made to C. Jacobi (jacobi@uni-leipzig.de). BLO data can be obtained from the Centre for Environmental Data Analysis (CEDA) online archive (Mitchell, 2019b). ASI data can be obtained online via the CEDA archive (Mitchell, 2019a). LEA data is available upon request from B. Fuller (bfuller@gsoft.com.au) and D. O'Connor (doconnor@gsoft.com.au). CAR, CPa, and SMa data can be requested from P.P. Batista (paulo.batista@inpe.br). CON data can be requested from A. Liu (liuz2@erau.edu). TdF data can be requested from D. Janches (diego.janches@nasa.gov). KEP data is available from the CEDA archive (Mitchell, 2021). Requests for access to the raw KSS data can be made to J.-H. Kim (jhkim@kopri.re.kr) and C. Lee (cslee@kopri.re.kr). ROT data is available from the CEDA archive (Mitchell, 2019c). DAV data can be requested from D. Murphy (Damian.Murphy@aad.gov.au). MCM data can be requested from S. Palo (Palo@colorado.edu).

Acknowledgments

ECMD, DJ, JDCS, and RSL are supported through the NASA ISFM programs for Heliophysics. GS is a member of the Oeschger Center for Climate Change Research. J-HK and CL were supported by a Korea Polar Research Institute (KOPRI) grant from the Ministry of Oceans and Fisheries (KOPRI PE24020). CJ acknowledges support by Deutsche Forschungsgemeinschaft (DFG) grant JA836/47-1. ML acknowledges support from UK Science and Technology Facilities Council grant ST/W00089X/1. TdF operation is supported by NESC assessment TI-17-01,204. ROT, and KEP radars were funded through UK Natural Environment Research Council grants NE/R001391 and NE/R001235/1. CPa, SMa, and CAR meteor radars were funded through São Paulo State Research Support Foundation and Brazilian National Research Conseil. DAV operation was supported by Australian Antarctic Science projects 2668, 4025, 4445 and 4637. Operation of KIR is provided by the Swedish Space Corporation (SSC) Esrange Space Center. AL is supported by (while serving at) the National Science Foundation, USA. Authors (DJ, GS, JK, MT, AK, ML, and AL) acknowledge discussions within the International Space Science Institute Team 23–580 "Meteors and Phenomena at the Boundary between Earth's Atmosphere and Outer Space." There are no real or perceived financial conflicts of interests for any author. We wish to thank the two anonymous reviewers whose comments lead to the strengthening and improvement of this manuscript.

References

Baumgarten, K., & Stober, G. (2019). On the evaluation of the phase relation between temperature and wind tides based on ground-based measurements and reanalysis data in the middle atmosphere. *Annales Geophysicae*, *37*(4), 581–602. https://doi.org/10.5194/angeo-37-581-2019

Becker, E., & Vadas, S. L. (2018). Secondary gravity waves in the winter mesosphere: Results from a high-resolution global circulation model. *Journal of Geophysical Research: Atmospheres*, *123*(5), 2605–2627. https://doi.org/10.1002/2017JD027460

Campbell-Brown, M. D., & Jones, J. (2006). Annual variation of sporadic radar meteor rates. *mnras*, *367*(2), 709–716. https://doi.org/10.1111/j.1365-2966.2005.09974.x

Carrillo-Sánchez, J. D., Bones, D. L., Douglas, K. M., Flynn, G. J., Wirick, S., Fegley, B., et al. (2020a). Injection of meteoric phosphorus into planetary atmospheres. *Planetary and Space Science*, *187*, 104926. https://doi.org/10.1016/j.pss.2020.104926

Carrillo-Sánchez, J. D., Gómez-Martín, J. C., Bones, D. L., Nesvorný, D., Pokorný, P., Benna, M., et al. (2020). Cosmic dust fluxes in the atmospheres of Earth, Mars, and Venus. *Icarus*, *335*, 113395. https://doi.org/10.1016/j.icarus.2019.113395

Carrillo-Sánchez, J. D., Nesvorný, D., Pokorný, P., Janches, D., & Plane, J. M. C. (2016). Sources of cosmic dust in the earth's atmosphere. *Geophysical Research Letters*, *43*(23). 2016GL071697. https://doi.org/10.1002/2016GL071697

Chau, J. L., Urco, J. M., Vierinen, J., Harding, B. J., Clahsen, M., Pfeffer, N., et al. (2021). Multistatic specular meteor radar network in Peru: System description and initial results. *Earth and Space Science*, *8*(1), e2020EA001293. https://doi.org/10.1029/2020ea001293

Clemesha, B., & Batista, P. (2006). The quantification of long-term atmospheric change via meteor ablation height measurements. *Journal of Atmospheric and Solar-Terrestrial Physics*, *68*(17), 1934–1939. https://doi.org/10.1016/j.jastp.2005.12.008

Dawkins, E. (2024). Seasonal and local time variation in the observed peak of the meteor altitude distributions by meteor radars (version 1.1) [dataset]. *Zenodo*. https://doi.org/10.5281/zenodo.12533628

Dawkins, E., Stober, G., Janches, D., Carrillo-Sánchez, J., Lieberman, R., Jacobi, C., et al. (2023). Solar cycle and long-term trends in the observed peak of the meteor altitude distributions by meteor radars. *Geophysical Research Letters*, *50*(2), e2022GL101953. https://doi.org/10.1029/2022gl101953

Dawkins, E. C., Stober, G., Carrillo-Sánchez, J. D., Janches, D., Weryk, R., Hormaechea, J. L., et al. (2023). A novel methodology to estimate pre-atmospheric dynamical conditions of small meteoroids. *Planetary and Space Science*, *238*, 105796. https://doi.org/10.1016/j.pss.2023.105796

De Wit, R., Hibbins, R., Espy, P., Orsolini, Y., Limpasuvan, V., & Kinnison, D. (2014). Observations of gravity wave forcing of the mesopause region during the January 2013 major sudden stratospheric warming. *Geophysical Research Letters*, *41*(13), 4745–4752. https://doi.org/10.1002/2014gl060501

De Wit, R., Janches, D., Fritts, D., Stockwell, R., & Coy, L. (2017). Unexpected climatological behavior of MLT gravity wave momentum flux in the lee of the Southern Andes hot spot. *Geophysical Research Letters*, *44*(2), 1182–1191. https://doi.org/10.1002/2016gl072311

Dunker, T., Hoppe, U.-P., Stober, G., & Rapp, M. (2013). Development of the mesospheric na layer at 69° n during the geminids meteor shower 2010. *Annales Geophysicae*, *31*(1), 61–73. https://doi.org/10.5194/angeo-31-61-2013

Fentzke, J. T., & Janches, D. (2008). A semi-empirical model of the contribution from sporadic meteoroid sources on the meteor input function observed at Arecibo. *Journal of Geophysical Research*, *113*(A03304). https://doi.org/10.1029/2007JA012531

Fentzke, J. T., Janches, D., & Sparks, J. J. (2009). Latitudinal and seasonal variability of the micrometeor input function: A study using model predictions, Arecibo, and PFISR observations. *Journal of Atmospheric and Solar-Terrestrial Physics*, *71*(6–7), 653–661. https://doi.org/10.1016/j.jastp.2008.07.015

Fritts, D. C., & Alexander, M. J. (2003). Gravity wave dynamics and effects in the middle atmosphere. *Reviews of Geophysics*, *41*(1), 1003. https://doi.org/10.1029/2001RG000106

Fritts, D. C., Janches, D., Iimura, H., Hocking, W. K., Mitchell, N. J., Stockwell, R. G., et al. (2010). Southern Argentina Agile Meteor Radar: System design and initial measurements of large-scale winds and tides. *Journal of Geophysical Research*, *115*(D18), 18112. https://doi.org/10.1029/2010JD013850

Harvey, V. L., Randall, C. E., Bailey, S. M., Becker, E., Chau, J. L., Cullens, C. Y., et al. (2022). Improving ionospheric predictability requires accurate simulation of the mesospheric polar vortex. *Frontiers in Astronomy and Space Sciences*, *9*. https://doi.org/10.3389/fspas.2022.1041426

Heale, C. J., & Snively, J. B. (2015). Gravity wave propagation through a vertically and horizontally inhomogeneous background wind. *Journal of Geophysical Research: Atmospheres*, *120*(12), 5931–5950. https://doi.org/10.1002/2015JD023505

Hervig, M. E., Malaspina, D., Sterken, V., Wilson, L. B., Hunziker, S., & Bailey, S. M. (2022). Decadal and annual variations in meteoric flux from ulysses, wind, and SOFIE observations. *Journal of Geophysical Research: Space Physics*, *127*(10), e2022JA030749. https://doi.org/10.1029/2022JA030749

Hocking, W. K., Fuller, B., & Vandepeer, B. (2001). Real-time determination of meteor-related parameters utilizing modern digital technology. *Journal of Atmospheric and Solar-Terrestrial Physics*, *63*(2–3), 155–169. https://doi.org/10.1016/s1364-6826(00)00138-3

Jacobi, C., Fröhlich, K., Viehweg, C., Stober, G., & Kürschner, D. (2007). Midlatitude mesosphere/lower thermosphere meridional winds and temperatures measured with meteor radar. *Advances in Space Research*, *39*(8), 1278–1283. https://doi.org/10.1016/j.asr.2007.01.003

Janches, D., Close, S., & Fentzke, J. T. (2008). A comparison of detection sensitivity between ALTAIR and Arecibo meteor observations: Can high power and large aperture radars detect low velocity meteor head-echoes. *Icarus*, *193*(1), 105–111. https://doi.org/10.1016/j.icarus.2007.08.022

Janches, D., Close, S., Hormaechea, J. L., Swarnalingam, N., Murphy, A., O'Connor, D., et al. (2015). The Southern Argentina Agile MEteor Radar Orbital System (SAAMER-OS): An initial sporadic meteoroid orbital survey in the southern sky. *Ap. J.*, *809*(1), 36. https://doi.org/10.1088/0004-637X/809/1/36

Janches, D., Dyrud, L. P., Broadley, S. L., & Plane, J. M. C. (2009). First observation of micrometeoroid differential ablation in the atmosphere. *Geophysical Research Letters*, *36*(6), 6101. https://doi.org/10.1029/2009GL037389

Janches, D., Palo, S., Lau, S., Avery, J., Avery, S., de la Peña, S., & Makarov, N. (2004). Diurnal and seasonal variability of the meteoric flux at the south pole measured with radars. *Geophysical Research Letters*, *31*(20). https://doi.org/10.1029/2004gl021104

Janches, D., Swarnalingam, J., Carrillo-Sanchez, N., Gomez-Martin, R., Marshall, J. C., Nesvorný, D., et al. (2017). Radar detectability studies of slow and small zodiacal dust cloud particles: III. The role of sodium and the head echo size on the probability of detection. *The Astrophysical Journal*, *843*(1), 11. https://doi.org/10.3847/1538-4357/aa775c

Jones, J., & Brown, P. (1993). Sporadic meteor radiant distribution: Orbital survey results. *Monthly Notices of the Royal Astronomical Society*, *265*(3), 524–532. https://doi.org/10.1093/mnras/265.3.524

Lima, L. M., Araújo, L. R., Alves, E., Batista, P. P., & Clemesha, B. R. (2015). Variations in meteor heights at 22.7 s during solar cycle 23. *Journal of Atmospheric and Solar-Terrestrial Physics*, *133*, 139–144. https://doi.org/10.1016/j.jastp.2015.08.015

Liu, A., Lu, X., & Franke, S. (2013). Diurnal variation of gravity wave momentum flux and its forcing on the diurnal tide. *Journal of Geophysical Research: Atmospheres*, *118*(4), 1668–1678. https://doi.org/10.1029/2012jd018653

Liu, G., Janches, D., Ma, J., Lieberman, R. S., Stober, G., Moffat-Griffin, T., et al. (2022). Mesosphere and lower thermosphere winds and tidal variations during the 2019 Antarctic sudden stratospheric warming. *Journal of Geophysical Research: Space Physics*, *127*(3), e2021JA030177. https://doi.org/10.1029/2021JA030177

Marino, J., Palo, S. E., & Rainville, N. (2022). First observations from a new meteor radar at McMurdo station Antarctica (77.8°S, 166.7°E). *Radio Science*, *57*(11), e2022RS007466. https://doi.org/10.1029/2022RS007466

Matthias, V., Stober, G., Kozlovsky, A., Lester, M., Belova, E., & Kero, J. (2021). Vertical structure of the arctic spring transition in the middle atmosphere. *Journal of Geophysical Research: Atmospheres*, *126*(10), e2020JD034353. https://doi.org/10.1029/2020JD034353

McCormack, J., Hoppel, K., Kuhl, D., de Wit, R., Stober, G., Espy, P., et al. (2017). Comparison of mesospheric winds from a high-altitude meteorological analysis system and meteor radar observations during the boreal winters of 2009–2010 and 2012–2013. *Journal of Atmospheric and Solar-Terrestrial Physics*, *154*, 132–166. https://doi.org/10.1016/j.jastp.2016.12.007

McKinley, D. W. R. (1961). *Meteor science and engineering*. McGraw Hill.

Mitchell, N. (2019a). University of bath: Ascension Island Skiymet Meteor radar data (2005-2012) [dataset]. *Centre for Environmental Data Analysis*. https://catalogue.ceda.ac.uk/uuid/0d05cf74e17f49c2b7c5cd02faa59291

Mitchell, N. (2019b). University of bath: Bear lake observatory Skiymet Meteor radar data (2008-2018) [dataset]. *Centre for Environmental Data Analysis*. https://catalogue.ceda.ac.uk/uuid/432c43bda95e4c3fa990e866ab78ad4f

Mitchell, N. (2019c). University of bath: Rothera Skiymet Meteor radar data (2005-present) [dataset]. https://catalogue.ceda.ac.uk/uuid/aa44e02718fd4ba49cefe36d884c6e50

Mitchell, N. (2021). University of bath: King Edward point Skiymet Meteor radar data (2016-2020) [dataset]. https://doi.org/10.5285/061fc7fd1ca940e7ad685daf146db08f

Mixa, T., Dörnbrack, A., & Rapp, M. (2021). Nonlinear simulations of gravity wave tunneling and breaking over Auckland Island. *Journal of the Atmospheric Sciences*, *78*(5), 1567–1582. https://doi.org/10.1175/JAS-D-20-0230.1

Nesvorný, D., Janches, D., Vokrouhlický, D., Pokorný, P., Bottke, W. F., & Jenniskens, P. (2011). Dynamical model for the zodiacal cloud and sporadic meteors. *The Astrophysical Journal*, *743*(2), 129. https://doi.org/10.1088/0004-637X/743/2/129

Nesvorný, D., Jenniskens, P., Levison, H. F., Bottke, W. F., Vokrouhlický, D., & Gounelle, M. (2010). Cometary origin of the zodiacal cloud and carbonaceous micrometeorites. Implications for hot debris disks. *The Astrophysical Journal*, *713*(2), 816–836. https://doi.org/10.1088/0004-637X/713/2/816

Olsson-Steel, D., & Elford, W. G. (1987). The height distribution of radio meteors: Observations at 2 MHz. *Journal of Atmospheric and Terrestrial Physics*, *49*(3), 243–258. https://doi.org/10.1016/0021-9169(87)90060-2

Öpik, E. J. (1958). *Physics of meteor flight in the atmosphere*. Interscience Publishers.

Plane, J. (2003). Atmospheric chemistry of meteoric metals. *Chemistry Review*, *103*(12), 4963–4984. https://doi.org/10.1021/cr0205309

Plane, J., Feng, W., & Dawkins, E. (2015). The mesosphere and metals: Chemistry and changes. *Chemistry Review*, *115*(10), 4497–4541. https://doi.org/10.1021/cr500501m

Pokorný, P., Vokrouhlický, D., Nesvorný, D., Campbell-Brown, M., & Brown, P. (2014). Dynamical model for the toroidal sporadic meteors. *The Astrophysical Journal*, *789*(1), 25. https://doi.org/10.1088/0004-637X/789/1/25

Poulter, E., & Baggaley, W. (1977). Radiowave scattering from meteoric ionization. *Journal of Atmospheric and Terrestrial Physics*, *39*(7), 757–768. https://doi.org/10.1016/0021-9169(77)90137-4

Rowan-Robinson, M., & May, B. (2013). An improved model for the infrared emission from the zodiacal dust cloud: Cometary, asteroidal and interstellar dust. *Monthly Notices of the Royal Astronomical Society*, *429*(4), 2894–2902. https://doi.org/10.1093/mnras/sts471

Schoeberl, M., & Newman, P. (2015). Middle atmosphere | polar vortex. In G. R. North, J. Pyle, & F. Zhang (Eds.), *Encyclopedia of atmospheric sciences* (2nd ed., pp. 12–17). Academic Press. https://doi.org/10.1016/B978-0-12-382225-3.00228-0

Schult, C., Stober, G., Janches, D., & Chau, J. L. (2017). Results of the first continuous meteor head echo survey at polar latitudes. *Icarus*, *297*, 1–13. https://doi.org/10.1016/j.icarus.2017.06.019

Sparks, J. J., & Janches, D. (2009). Latitudinal dependence of the variability of the micrometeor altitude distribution. *Geophysical Research Letters*, *36*(12), 12105. https://doi.org/10.1029/2009GL038485

Stober, G., Baumgarten, K., McCormack, J. P., Brown, P., & Czarnecki, J. (2020). Comparative study between ground-based observations and NAVGEM-HA analysis data in the mesosphere and lower thermosphere region. *Atmospheric Chemistry and Physics*, *20*(20), 11979–12010. Retrieved from https://doi.org/10.5194/acp-20-11979-2020

Stober, G., Brown, P., Campbell-Brown, M., & Weryk, R. (2021). Triple-frequency meteor radar full wave scattering - Measurements and comparison to theory. *Astronomy & Astrophysics*, *654*, A108. https://doi.org/10.1051/0004-6361/202141470

Stober, G., Jacobi, C., Matthias, V., Hoffmann, P., & Gerding, M. (2012). Neutral air density variations during strong planetary wave activity in the mesopause region derived from meteor radar observations. *Journal of Atmospheric and Solar-Terrestrial Physics*, *74*, 55–63. https://doi.org/10.1016/j.jastp.2011.10.007

Stober, G., Janches, D., Matthias, V., Fritts, D., Marino, J., Moffat-Griffin, T., et al. (2021). Seasonal evolution of winds, atmospheric tides, and Reynolds stress components in the southern hemisphere mesosphere–lower thermosphere in 2019. *Annales Geophysicae*, *39*(1), 1–29. https://doi.org/10.5194/angeo-39-1-2021

Stober, G., Kuchar, A., Pokhotelov, D., Liu, H., Liu, H.-L., Schmidt, H., et al. (2021). Interhemispheric differences of mesosphere–lower thermosphere winds and tides investigated from three whole-atmosphere models and meteor radar observations. *Atmospheric Chemistry and Physics*, *21*(18), 13855–13902. https://doi.org/10.5194/acp-21-13855-2021

Stober, G., Liu, A., Kozlovsky, A., Qiao, Z., Kuchar, A., Jacobi, C., et al. (2022). Meteor radar vertical wind observation biases and mathematical debiasing strategies including the 3dvar+ div algorithm. *Atmospheric Measurement Techniques*, *15*(19), 5769–5792. https://doi.org/10.5194/amt-15-5769-2022

Stober, G., Matthias, V., Brown, P., & Chau, J. (2014). Neutral density variation from specular meteor echo observations spanning one solar cycle. *Geophysical Research Letters*, *41*(19), 6919–6925. https://doi.org/10.1002/2014gl061273

Stober, G., Weryk, R., Janches, D., Dawkins, E. C., Günzkofer, F., Hormaechea, J. L., & Pokhotelov, D. (2023). Polarization dependency of transverse scattering and collisional coupling to the ambient atmosphere from meteor trails — Theory and observations. *Planetary and Space Science*, *237*, 105768. https://doi.org/10.1016/j.pss.2023.105768

Vadas, S. L., & Becker, E. (2018). Numerical modeling of the excitation, propagation, and dissipation of primary and secondary gravity waves during wintertime at McMurdo station in the Antarctic. *Journal of Geophysical Research: Atmospheres*, *123*(17), 9326–9369. https://doi.org/10.1029/2017JD027974

Vadas, S. L., Zhao, J., Chu, X., & Becker, E. (2018). The excitation of secondary gravity waves from local body forces: Theory and observation. *Journal of Geophysical Research: Atmospheres*, *123*(17), 9296–9325. https://doi.org/10.1029/2017JD027970

Vondrak, T., Plane, J. M. C., Broadley, S., & Janches, D. (2008). A chemical model of meteoric ablation. *Atmospheric Chemistry and Physics*, *8*(23), 7015–7031. https://doi.org/10.5194/acp-8-7015-2008

Zook, H. A. (2001). Spacecraft measurements of the cosmic dust flux. In *Accretion of extraterrestrial matter throughout Earth's history* (pp. 75–92). https://doi.org/10.1007/978-1-4419-8694-8_5